The Astrophysical Journal, 690:1236–1249, 2009 January 10 doi:10.1088/0004-637X/690/2/1236


# COSMOS PHOTOMETRIC REDSHIFTS WITH 30-BANDS FOR 2-deg$^2$

O. Ilbert[1], P. Capak[2,3], M. Salvato[2], H. Aussel[4], H. J. McCracken[5], D. B. Sanders[1], N. Scoville[2], J. Kartaltepe[1], S. Arnouts[6], E. Le Floc'h[1], B. Mobasher[7], Y. Taniguchi[8], F. Lamareille[9], A. Leauthaud[10], S. Sasaki[11,12], D. Thompson[2,13], M. Zamojski[2], G. Zamorani[14], S. Bardelli[14], M. Bolzonella[14], A. Bongiorno[10], M. Brusa[15], K. I. Caputi[16], C. M. Carollo[16], T. Contini[9], R. Cook[2], G. Coppa[14], O. Cucciati[17], S. de la Torre[11], L. de Ravel[11], P. Franzetti[18], B. Garilli[18], G. Hasinger[15], A. Iovino[17], P. Kampczyk[16], J.-P. Kneib[10], C. Knobel[16], K. Kovac[16], J. F. Le Borgne[9], V. Le Brun[10], O. Le Fèvre[11], S. Lilly[16], D. Looper[1], C. Maier[16], V. Mainieri[9], Y. Mellier[5], M. Mignoli[14], T. Murayama[12], R. Pellò[9], Y. Peng[16], E. Pérez-Montero[9], A. Renzini[19], E. Ricciardelli[19], D. Schiminovich[20], M. Scodeggio[18], Y. Shioya[8], J. Silverman[16], J. Surace[3], M. Tanaka[21], L. Tasca[10], L. Tresse[10], D. Vergani[18], and E. Zucca[14]

[1] Institute for Astronomy, 2680 Woodlawn Dr., University of Hawaii, Honolulu, HI 96822, USA
[2] California Institute of Technology, MC 105-24, 1200 East California Boulevard, Pasadena, CA 91125, USA
[3] *Spitzer* Science Center, California Institute of Technology, Pasadena, CA 91125, USA
[4] AIM Unité Mixte de Recherche CEA CNRS, Université Paris VII UMR n158, Paris, France
[5] Institut d'Astrophysique de Paris, UMR7095 CNRS, Université Pierre et Marie Curie, 98 bis Boulevard Arago, 75014 Paris, France
[6] Canada–France–Hawaii Telescope Corporation, 65-1238 Mamalahoa Hwy, Kamuela, HI 96743, USA
[7] Department of Physics and Astronomy, University of California, Riverside, CA 92521, USA
[8] Research Center for Space and Cosmic Evolution, Ehime University, Bunkyo-cho, Matsuyama 790-8577, Japan
[9] Max Planck Institut für Extraterrestrische Physik, D-85478 Garching, Germany
[10] Laboratoire d'Astrophysique de Toulouse/Tarbes, Université de Toulouse, CNRS, 14 Avenue E. Belin, 31400 Toulouse, France
[11] Laboratoire d'Astrophysique de Marseille, B.P. 8, Traverse du Siphon, 13376 Marseille Cedex 12, France
[12] Astronomical Institute, Graduate School of Science, Tohoku University, Aramaki, Aoba, Sendai 980-8578, Japan
[13] Physics Department, Graduate School of Science & Engineering, Ehime University, 2-5 Bunkyo-cho, Matsuyama 790-8577, Japan
[14] Large Binocular Telescope Observatory, University of Arizona, 933 N. Cherry Ave., Tucson, AZ 85721-0065, USA
[15] INAF-Osservatorio Astronomico di Bologna, via Ranzani 1, I-40127 Bologna, Italy
[16] Department of Physics, ETH Zurich, CH-8093 Zurich, Switzerland
[17] INAF-Osservatorio Astronomico di Brera, Milano, Italy
[18] INAF-IASF Milano, via Bassini 15, 20133 Milano, Italy
[19] Dipartimento di Astronomia, Università di Padova, vicolo dell'Osservatorio 2, I-35122 Padua, Italy
[20] Department of Astronomy, Columbia University, MC2457, 550 W. 120 Street, New York, NY 10027, USA
[21] European Southern Observatory, Karl-Schwarzschild-Str. 2, D-85748 Garching, Germany
*Received 2008 August 15; accepted 2008 September 10; published 2008 December 8*

## ABSTRACT

We present accurate photometric redshifts (photo-z) in the 2-deg$^2$ COSMOS field. The redshifts are computed with 30 broad, intermediate, and narrowbands covering the UV (*Galaxy Evolution Explorer*), visible near-IR (NIR; Subaru, Canada–France–Hawaii Telescope (CFHT), United Kingdom Infrared Telescope, and National Optical Astronomy Observatory), and mid-IR (*Spitzer*/IRAC). A $\chi^2$ template-fitting method (*Le Phare*) was used and calibrated with large spectroscopic samples from the Very Large Telescope Visible Multi-Object Spectrograph and the Keck Deep Extragalactic Imaging Multi-Object Spectrograph. We develop and implement a new method which accounts for the contributions from emission lines ([O II], H$\beta$, H$\alpha$, and Ly$\alpha$) to the spectral energy distributions (SEDs). The treatment of emission lines improves the photo-z accuracy by a factor of 2.5. Comparison of the derived photo-z with 4148 spectroscopic redshifts (i.e., $\Delta z = z_s - z_p$) indicates a dispersion of $\sigma_{\Delta z/(1+z_s)} = 0.007$ at $i^+_{AB} < 22.5$, a factor of 2–6 times more accurate than earlier photo-z in the COSMOS, CFHT Legacy Survey, and the Classifying Object by Medium-Band Observations-17 survey fields. At fainter magnitudes $i^+_{AB} < 24$ and $z < 1.25$, the accuracy is $\sigma_{\Delta z/(1+z_s)} = 0.012$. The deep NIR and Infrared Array Camera coverage enables the photo-z to be extended to $z \sim 2$, albeit with a lower accuracy ($\sigma_{\Delta z/(1+z_s)} = 0.06$ at $i^+_{AB} \sim 24$). The redshift distribution of large magnitude-selected samples is derived and the median redshift is found to range from $z_m = 0.66$ at $22 < i^+_{AB} < 22.5$ to $z_m = 1.06$ at $24.5 < i^+_{AB} < 25$. At $i^+_{AB} < 26.0$, the multiwavelength COSMOS catalog includes approximately 607,617 objects. The COSMOS-30 photo-z enables the full exploitation of this survey for studies of galaxy and large-scale structure evolution at high redshift.

*Key words:* galaxies: distances and redshifts – galaxies: evolution – galaxies: formation

*Online-only material:* color figures

## 1. INTRODUCTION

Photometric redshifts (photo-z) are an estimate of galaxy distances based on the observed colors (Baum 1962). This method is extremely efficient for assembling large redshift samples for faint galaxies. Despite having a lower accuracy than spectroscopic redshifts (spectro-z), photo-z have the advantage of significantly improved completeness down to a flux limit fainter than the spectroscopic limit. Deep photo-z samples, such as the Classifying Object by Medium-Band Observations-17 (COMBO-17; Wolf et al. 2003) Canada–France–Hawaii Telescope Legacy Survey (CFHTLS; Ilbert et al. 2006),

*Spitzer* Wide-field Infrared Extragalactic (SWIRE) Survey (Rowan-Robinson et al. 2008), and COSMOS (Mobasher et al. 2007), contain more than 1,000,000 galaxies and go as faint as $i \sim 25$ with a relatively small amount of telescope time.

Typical photo-z with an accuracy of $\sigma_{\Delta z/(1+z_s)} \sim 0.02$–$0.04$ ($\Delta z = z_s - z_p$) are widely used to study the evolution of galaxy stellar masses and luminosities (e.g., Fontana et al. 2000; Wolf et al. 2003; Gabasch et al. 2004; Caputi et al. 2006; Arnouts et al. 2007), for angular clustering analysis (e.g., Heinis et al. 2007; McCracken et al. 2007), to study the relation between galaxy properties and environment (e.g., Capak et al. 2007), to trace large-scale structures (Mazure et al. 2007; Scoville et al. 2007), and to identify clusters at high redshift (Wang & Steinhardt 1998). Photo-z are also necessary for dark energy and dark matter weak-lensing studies to separate foreground and background galaxies and to control systematic effects such as intrinsic shape alignment, shear shape correlation, and the effects of source clustering (Peacock et al. 2006). All of these applications require strict control of systematic effects in the photo-z estimate. An efficient way of identifying and removing systematics is to calibrate photo-z on a spectroscopic sample. The most common methods of calibration are neural network methods (e.g., Ball et al. 2004; Collister & Lahav 2004), a calibration of the color–$z$ relation (Brodwin et al. 2006; Ilbert et al. 2006), or a reconstruction of the spectral energy distribution (SED) templates (Budavári et al. 2000; Feldmann et al. 2006).

As is also true for spectro-z measurements, photo-z accuracy depends on spectral coverage and resolution. It is also degraded for sources with a low signal-to-noise ratio (S/N; Bolzonella et al. 2000). The Balmer and Lyman breaks contain much of the photo-z information, so accuracy is lower in redshift ranges where these features are not well sampled by the filter set. As the photometric accuracy degrades, it becomes more difficult to constrain the positions of these features, leading to lower accuracy. This creates a dual dependency of photo-z accuracy on magnitude and redshift which is defined by the survey design (exposure time, filter choice, and calibration accuracy). For this reason, any photo-z sample should be extensively tested and characterized in the same way a spectroscopic sample would be. This analysis is necessary in order to identify the redshift/magnitude ranges over which the photo-z can be trusted and used for a given scientific application.

This paper presents a new version of the photo-z for the Cosmic Evolution Survey (COSMOS; Scoville et al. 2007) and an analysis of their accuracy. COSMOS is the largest *Hubble Space Telescope (HST)* survey ever undertaken—imaging an equatorial 2-deg$^2$ field to a depth of $I_{F814W} = 27.8$ mag ($5\sigma$; AB). The COSMOS field is equatorial to ensure visibility by all ground-based astronomical facilities. This project includes extensive multiwavelength imaging from X-ray to radio (*XMM*, *Chandra*, *Galaxy Evolution Explorer* (*GALEX*), Subaru, Canada–France–Hawaii Telescope (CFHT), United Kingdom Infrared Telescope (UKIRT), *Spitzer*, VLA). New ground-based NIR data (H. J. McCracken et al. 2008, in preparation; P. Capak et al. 2008, in preparation), *Spitzer*-IRAC data (Sanders et al. 2007), and medium/narrowband data from the Subaru Telescope (Taniguchi et al. 2007; S. Sasaki et al. 2008, in preparation; Y. Taniguchi et al. 2008, in preparation; P. Capak et al. 2008, in preparation) greatly improve the previous photometry catalog (Capak et al. 2007). These new data are used for the photo-z derived here, yielding a factor of 3 higher accuracy than the first release of COSMOS photo-z (Mobasher et al. 2007).

The COSMOS data are presented in Section 2. The technique used to estimate the photo-z is presented in Section 3. In Section 4, we quantify the photo-z accuracy as a function of the magnitude and redshift. In Section 5, we provide the photo-z distribution of the $i^+$ selected samples. Specialized photo-z for X-ray selected sources, active galactic nucleus (AGN), and variable objects are discussed in a companion paper (Salvato et al. 2008).

Throughout this paper, we use the standard *WMAP* cosmology ($\Omega_m = 0.3$, $\Omega_\Lambda = 0.7$) with $h = 0.7$ and $h = H_0/100$ km s$^{-1}$ Mpc$^{-1}$. Magnitudes are given in the AB system.

## 2. DATA

Compared with the previous optical/NIR catalog (Capak et al. 2007), the new photometry implements 14 new medium/narrowband data from the Subaru Telescope, deep ground-based NIR data ($J$ and $K$ bands), and *Spitzer*-IRAC data. The spectroscopic sample used to calibrate/test the photo-z is 10 times larger at $i^+_{AB} < 22.5$ than that of Mobasher et al. (2007). The spectroscopic sample is supplemented with faint IR selected sources and a deep, faint spectroscopic sample at $z > 1.5$. Hereafter, we detail the photometric and spectroscopic data used to measure the photo-z.

### 2.1. Photometric Data

Fluxes are measured in 30 bands from data taken on the Subaru (4200–9000 Å), CFHT (3900–21500 Å), UKIRT (12500 Å), *Spitzer* (3.6–8 $\mu$m), and *GALEX* (1500–2300 Å) telescopes. We refer to P. Capak et al. (2008, in preparation) for a complete description of the observations, data reduction, and the photometry catalog. The equivalent width and the effective wavelength of each filter are listed in Table 1. The sensitivities are given by P. Capak et al. (2008, in preparation) and in Table 1 of Salvato et al. (2008). Table 1 indicates the fraction of sources detected in each band with an error less than 0.2 mag for a selection at $i^+ < 24.5$, $i^+ < 25$, and $i^+ < 25.5$. We summarize below the datasets used in this paper.

1. **UV:** Very deep $u^*$ band data were obtained at the 3.6 m CFHT using the Megacam camera (Boulade et al. 2003). The $u^*$ band data were processed at the TERAPIX data reduction center.[22] The $u^*$ band data cover the entire COSMOS field and reach a depth of $u^* \sim 26.5$ mag for a point source detected at $5\sigma$. The $u^*$ band images are also used as priors in the measurement of FUV (1500 Å) and NUV (2300 Å) fluxes in order to ensure a proper deblending of sources in the *GALEX* images (Zamojski et al. 2007). *GALEX* fluxes are then extracted using the EM-algorithm (Guillaume et al. 2006). They reach a depth of FUV $\sim 26$ mag and NUV $\sim 25.7$ mag.
2. **Optical:** The COSMOS-20 survey (Y. Taniguchi et al. 2008, in preparation) entailed 30 nights of observation at the Subaru 8.2 m telescope using the Suprime-Cam instrument. The observations are complete in 20 bands: six broadbands ($B_J$, $V_J$, $g^+$, $r^+$, $i^+$, $z^+$), 12 medium bands ($IA427$, $IA464$, $IA484$, $IA505$, $IA527$, $IA574$, $IA624$, $IA679$, $IA709$, $IA738$, $IA767$, $IA827$), and two narrowbands ($NB711$, $NB816$).

[22] terapix.iap.fr

3. **NIR:** The catalog includes deep $J$ and $K$ band data obtained using the WFCAM and WIRCAM wide-field infrared cameras on UKIRT and CFHT, respectively. The NIR data reduction is detailed by P. Capak et al. (2008, in preparation) and H. J. McCracken et al. (2008, in preparation). The data reach $J \sim 23.7$ mag and $K \sim 23.7$ mag for a point source detected at $5\sigma$.
4. **Mid-IR:** Deep IRAC data were taken during the *Spitzer* cycle 2 S-COSMOS survey (Sanders et al. 2007). A total of 166 hr were dedicated to cover the full 2-deg$^2$ with the IRAC camera in four bands: 3.6 $\mu$m, 4.5 $\mu$m, 5.6 $\mu$m, and 8.0 $\mu$m. Source detection is based on the 3.6 $\mu$m image and the fluxes were measured in the four IRAC bands using the "dual mode" configuration of SExtractor. The IRAC catalog is 50% complete at 1 $\mu$Jy at 3.6 $\mu$m ($m_{3.6\,\mu\mathrm{m}} \sim 23.9$ mag).

All of the imaging data were combined to generate a master photometry catalog (P. Capak et al. 2008, in preparation). Photometry was done using SExtractor in dual mode (Bertin & Arnouts 1996). Source detection was run on the deepest image ($i^+ \sim 26.2$ for a point source detected at $5\sigma$). For the UV-NIR data, the point-spread function (PSF) varies from 0.″5 to 1.″5 from the $K$ to the $u^*$ images. In order to obtain accurate colors, all the images were degraded to the same PSF of 1.″5 following the method described by Capak et al. (2007). The final photometry catalog contains PSF-matched photometry for all the bands from the $u^*$ to the $K$ band, measured over an aperture of 3″ diameter at the position of the $i^+$ band detection. For the FUV and NUV data, we transformed the total flux provided for the *GALEX*-FUV and -NUV counterpart by multiplying it by a factor of 0.759. This factor is the fraction of the flux observed in optical into a 3″ aperture flux as determined for point sources from simulations by Capak et al. (2007). To compensate for this approximation, we add in quadrature 0.1 and 0.3 mag to all the measured errors in the *GALEX*-NUV and -FUV bands.

For the mid-IR data we did not degrade the optical data to the larger IRAC PSF. Instead, the following procedures were used. An IRAC flux was first associated with the optical sources by matching their positions in each of the four IRAC bands within a search radius of 1″. Following Surace et al. (2004), the IRAC fluxes were then measured in a circular aperture of radius 1.″9. The aperture flux was then converted to a total flux using the aperture correction factors 0.76, 0.74, 0.62, and 0.58 at 3.6 $\mu$m, 4.5 $\mu$m, 5.6 $\mu$m, and 8.0 $\mu$m, respectively (Surace et al. 2004). Since the optical fluxes were measured over an aperture of 3″ diameter which encloses ∼75% of the flux for a point-like source, we then multiply the IRAC total fluxes by a factor of 0.75. This approximation provides good agreement between the predicted and observed colors ($z^+ - 3.6\,\mu$m and $3.6\,\mu\mathrm{m} - 4.5\,\mu$m colors). In order to compensate for this approximation, we add in quadrature 0.1, 0.1, 0.3, and 0.3 mag to the errors in the IRAC 3.6, 4.5, 5.6, and 8.0 $\mu$m, respectively.

Finally, all magnitudes are corrected for galactic extinction, estimated for each object individually using dust map images from Schlegel et al. (1998). We limit the photo-z analysis to an area of 2-deg$^2$ ($149.41140 < \alpha < 150.826934$ and $1.49878 < \delta < 2.91276$) which has a uniform and deep coverage in all the bands. Poor image quality areas (e.g., field boundary, saturated stars, satellite tracks, and image defects) are masked. Photo-z are computed only in the non-masked regions with a total covered area of 1.73 deg$^2$. There are 126,071, 293,627, and 607,617 sources detected at $i^+ < 24$, $i^+ < 25$, and $i^+ < 26$, respectively.

**Table 1**
Effective Wavelength, Width, and Systematic Offsets[a], $s_f$, in Magnitude. Plus the Fraction of Sources in Each Band With an Error Less Than 0.2 mag at $i^+ < 24.5$, $i^+ < 25$, $i^+ < 25.5$

| Filter | Telescope | Effective λ | FWHM | $s_f$ | % at $i^+ < 24.5$ | % at $i^+ < 25$ | % at $i^+ < 25.5$ |
|---|---|---|---|---|---|---|---|
| $u^*$ | CFHT | 3911.0 | 538.0 | 0.054 | 89.3 | 85.2 | 77.2 |
| $B_J$ | Subaru | 4439.6 | 806.7 | −0.242 | 97.1 | 95.2 | 90.5 |
| $V_J$ | Subaru | 5448.9 | 934.8 | −0.094 | 99.3 | 98.2 | 94.2 |
| $g^+$ | Subaru | 4728.3 | 1162.9 | 0.024 | 96.4 | 93.6 | 86.0 |
| $r^+$ | Subaru | 6231.8 | 1348.8 | 0.003 | 99.6 | 99.5 | 98.4 |
| $i^+$ | Subaru | 7629.1 | 1489.4 | 0.019 | 99.9 | 99.9 | 99.8 |
| $i*$ | CFHT | 7628.9 | 1460.0 | −0.007 | 37.8 | 25.4 | 17.4 |
| $z^+$ | Subaru | 9021.6 | 955.3 | −0.037 | 99.8 | 97.9 | 83.8 |
| $J$ | UKIRT | 12444.1 | 1558.0 | 0.124 | 65.4 | 49.1 | 35.7 |
| $K_S$ | NOAO | 21434.8 | 3115.0 | 0.022 | 15.3 | 10.3 | 7.08 |
| $K$ | CFHT | 21480.2 | 3250.0 | −0.051 | 84.1 | 68.5 | 52.1 |
| $IA427$ | Subaru | 4256.3 | 206.5 | 0.037 | 77.1 | 64.3 | 48.4 |
| $IA464$ | Subaru | 4633.3 | 218.0 | 0.013 | 78.5 | 64.3 | 47.6 |
| $IA484$ | Subaru | 4845.9 | 228.5 | 0.000 | 88.7 | 78.3 | 62.0 |
| $IA505$ | Subaru | 5060.7 | 230.5 | −0.002 | 84.0 | 70.0 | 52.0 |
| $IA527$ | Subaru | 5258.9 | 242.0 | 0.026 | 93.2 | 84.6 | 68.7 |
| $IA574$ | Subaru | 5762.1 | 271.5 | 0.078 | 92.5 | 80.0 | 60.6 |
| $IA624$ | Subaru | 6230.0 | 300.5 | 0.002 | 97.4 | 90.2 | 72.2 |
| $IA679$ | Subaru | 6778.8 | 336.0 | −0.181 | 99.5 | 96.7 | 82.9 |
| $IA709$ | Subaru | 7070.7 | 315.5 | −0.024 | 99.8 | 97.7 | 83.5 |
| $IA738$ | Subaru | 7358.7 | 323.5 | 0.017 | 99.5 | 94.2 | 73.6 |
| $IA767$ | Subaru | 7681.2 | 364.0 | 0.041 | 99.6 | 93.5 | 72.0 |
| $IA827$ | Subaru | 8240.9 | 343.5 | −0.019 | 99.7 | 97.2 | 81.8 |
| $NB711$ | Subaru | 7119.6 | 72.5 | 0.014 | 84.8 | 60.7 | 41.9 |
| $NB816$ | Subaru | 8149.0 | 119.5 | 0.068 | 99.8 | 99.1 | 88.2 |
| $IRAC1$ | *Spitzer* | 35262.5 | 7412.0 | 0.002 | 70.6 | 60.8 | 48.4 |
| $IRAC2$ | *Spitzer* | 44606.7 | 10113.0 | 0.000 | 62.6 | 51.6 | 39.7 |
| $IRAC3$ | *Spitzer* | 56764.4 | 13499.0 | 0.013 | 33.7 | 26.0 | 19.5 |
| $IRAC4$ | *Spitzer* | 77030.1 | 28397.0 | −0.171 | 15.7 | 11.3 | 8.1 |
| *FUV* | *GALEX* | 1551.3 | 230.8 | 0.314 | 8.5 | 5.8 | 4.0 |
| *NUV* | *GALEX* | 2306.5 | 789.1 | −0.022 | 19.7 | 13.4 | 9.2 |

**Note.** [a] With our definition, $s_f$ have the opposite sign to Table 13 of Capak et al. (2007).

### 2.2. Spectroscopic Data

The spectroscopic samples were observed with the Very Large Telescope (VLT) Visible Multi-Object Spectrograph (VIMOS) spectrograph (zCOSMOS; Lilly et al. 2007) and the Keck Deep Extragalactic Imaging Multi-Object Spectograph (DEIMOS) spectrograph (J. Kartaltepe et al. 2008, in preparation). These two spectroscopic samples have very different selection criteria (see below); they therefore cover very different ranges of redshift and color space, providing a broad sample for evaluation of the photo-z.

The zCOSMOS survey (Lilly et al. 2007) has two components: zCOSMOS-bright with a sample of 20,000 galaxies selected at $i^* \leqslant 22.5$ and zCOSMOS-faint with approximately 10,000 galaxies color-selected to lie in the redshift range $1.5 \lesssim z \lesssim 3$. In the latter, galaxies are selected by color based either on the $BzK$ criterion (Daddi et al. 2004) or the $UGR$ "BM" and "BX" criterion of Steidel et al. (2004), and the magnitude cut was $B_J < 24$–25 (depending on the color cut). zCOSMOS-bright galaxies were observed using the red grism of VIMOS covering a wavelength range 5500 Å $< \lambda <$ 9000 Å at a resolution of 600 (MR grism). For the zCOSMOS-faint sample, observations were carried out with the blue grism of VIMOS (3600 Å $< \lambda <$ 6800 Å) at a resolution of 200.

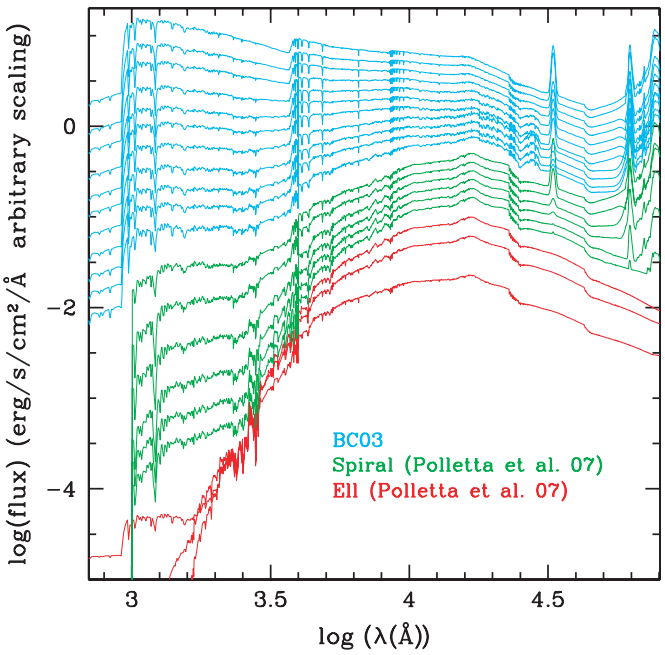


**Figure 1.** SED templates. The flux scale is arbitrary. The top 12 SEDs (cyan) are generated with BC03. The spiral (green) and elliptical (red) SEDs are from Polletta et al. (2007).

(A color version of this figure is available in the online journal.)

The zCOSMOS-bright survey is now ∼50% complete. Here we make use of only the extremely secure spectro-z measurements with a confidence level greater than 99% (class 3 and 4). This secure zCOSMOS-bright sample contains 4148 galaxies with a median redshift of ∼0.48. The zCOSMOS-faint survey is in its early stages, and here we use a preliminary sample of 148 galaxies with a median redshift of $z_m \sim 2.2$ and as faint as $i^+ \sim 25$. This zCOSMOS-faint spectroscopic sample is not fully representative of the average population at $1.5 < z < 3$ due to the selection criteria (e.g., $B_J < 24$–25).

The Keck II spectroscopic follow-up of 24 $\mu$m selected sources (J. Kartaltepe et al. 2008, in preparation) is ongoing and we refer to this sample as MIPS-spectro-z. The DEIMOS spectra cover a wavelength range 4000 Å $< \lambda <$ 9000 Å at a resolution of 600. This sample of 24 $\mu$m selected galaxies contains 317 secure spectro-z (at least two spectral features) with an average redshift of $z \sim 0.74$ and apparent magnitude in the range $18 < i^+ < 25$.

For all of the spectroscopic samples used in this paper for testing and verification of the photo-z, we include only secure spectro-z. Therefore, the uncertainties in the spectro-z are neglected and the spectro-z are used as a reference to assess the quality of the photo-z.

## 3. PHOTO-Z DERIVATION

Photo-z were derived using the *Le Phare* code[23] (S. Arnouts & O. Ilbert) which is based on a $\chi^2$ template-fitting procedure. In the discussion below, we focus on the improvements introduced here as compared to Ilbert et al. (2006) and the previous COSMOS photo-z (Mobasher et al. 2007).

### 3.1. Galaxy SED Template Library

Ilbert et al. (2006) and Mobasher et al. (2007) used a set of local galaxy SED templates (Coleman et al. 1980, hereafter CWW) which have been widely employed for photo-z (e.g., Sawicki et al. 1997; Fernández-Soto et al. 1999; Arnouts et al. 1999; Brodwin et al. 2006). Here, we employ a new set of templates generated by Polletta et al. (2007) with the code GRASIL (Silva et al. 1998). Polletta et al. selected their templates for fitting the VIMOS VLT Deep Survey (VVDS) sources (Le Fèvre et al. 2005) from the UV-optical (CFHTLS; McCracken et al. 2007) to the mid-IR (SWIRE; Lonsdale et al. 2003). Therefore, this set of templates provides a better joining of UV and mid-IR than those by CWW. The nine galaxy templates of Polletta et al. (2007) include three SEDs of elliptical galaxies and six templates of spiral galaxies (S0, Sa, Sb, Sc, Sd, Sdm).

We did find that the blue observed colors of the spectroscopic sample were not fully reproduced by the Polletta et al. (2007) templates. We therefore generated 12 additional templates using Bruzual & Charlot (2003, hereafter BC03) models with starburst (SB) ages ranging from 3 to 0.03 Gyr. We extend the BC03 templates beyond 3 $\mu$m rest-frame using the Sdm template of Polletta et al. (2007). The full library of template SEDs, nine from Polletta et al. (2007) and 12 from BC03, is shown in Figure 1. Finally, we linearly interpolated between some Polletta et al. templates to refine the sampling in color–$z$ space.

Figure 2 shows the observed colors and redshifts of the spectroscopic sample compared with the predicted colors for the library SEDs.

### 3.2. Emission Lines

Figure 2 clearly shows how the observed colors oscillate with the redshift, especially when the colors are measured with the medium bands (top panels). Comparing the template curves with (dashed) and without (solid) emission lines, one sees that the expected line fluxes can cause up to 0.4 mag changes in the color. This effect is particularly important when colors involving intermediate and narrowband filters are computed (see, for example, the upper right panel in Figure 2) but can be already noticed using broadband colors. The color oscillations are well explained by the contribution of emission lines like H$\alpha$, [O III], and [O II] to the observed flux, thus the contribution of the emission lines to the flux must be taken into account to obtain accurate photo-z; this is a major change implemented here compared with Ilbert et al. (2006) and Mobasher et al. (2007).

In order to include the emission line contribution to the SED, we need to model the emission line fluxes (O II, O III, H$\beta$, H$\alpha$, Ly$\alpha$) at any redshift, template, and extinction. The rescaling of the template ($A$ in Equation (2)) determines also the emission line fluxes (therefore, the modeling of the fluxes must be done galaxy by galaxy).

Our new procedure estimates the [O II] emission line flux from the UV luminosity of the rescaled template, using the Kennicutt (1998) calibration laws. In the template fitting, a UV rest-frame luminosity corrected for dust extinction can be computed at every step of the redshift/template/extinction grid (the rescaling factor $A$ is taken into account in the UV luminosity). The UV luminosity (at 2300 Å) is then related to the star formation rate (SFR) using the relation SFR ($M_\odot$ yr$^{-1}$) = $1.4 \times 10^{-28} L_\nu$ (erg s$^{-1}$ Hz$^{-1}$) from Kennicutt (1998). This SFR can then be translated to an [O II] emission line flux using the relation SFR ($M_\odot$ yr$^{-1}$) = $(1.4 \pm 0.4) \times 10^{-41} L_{[O\,II]}$ (erg s$^{-1}$) (Kennicutt 1998). This translates to

$$\log(F_{[O\,II]}) = -0.4 \times M_{UV} + 10.65 - \frac{DM(z)}{2.5}, \quad (1)$$

[23] www.oamp.fr/people/arnouts/LE_PHARE.html

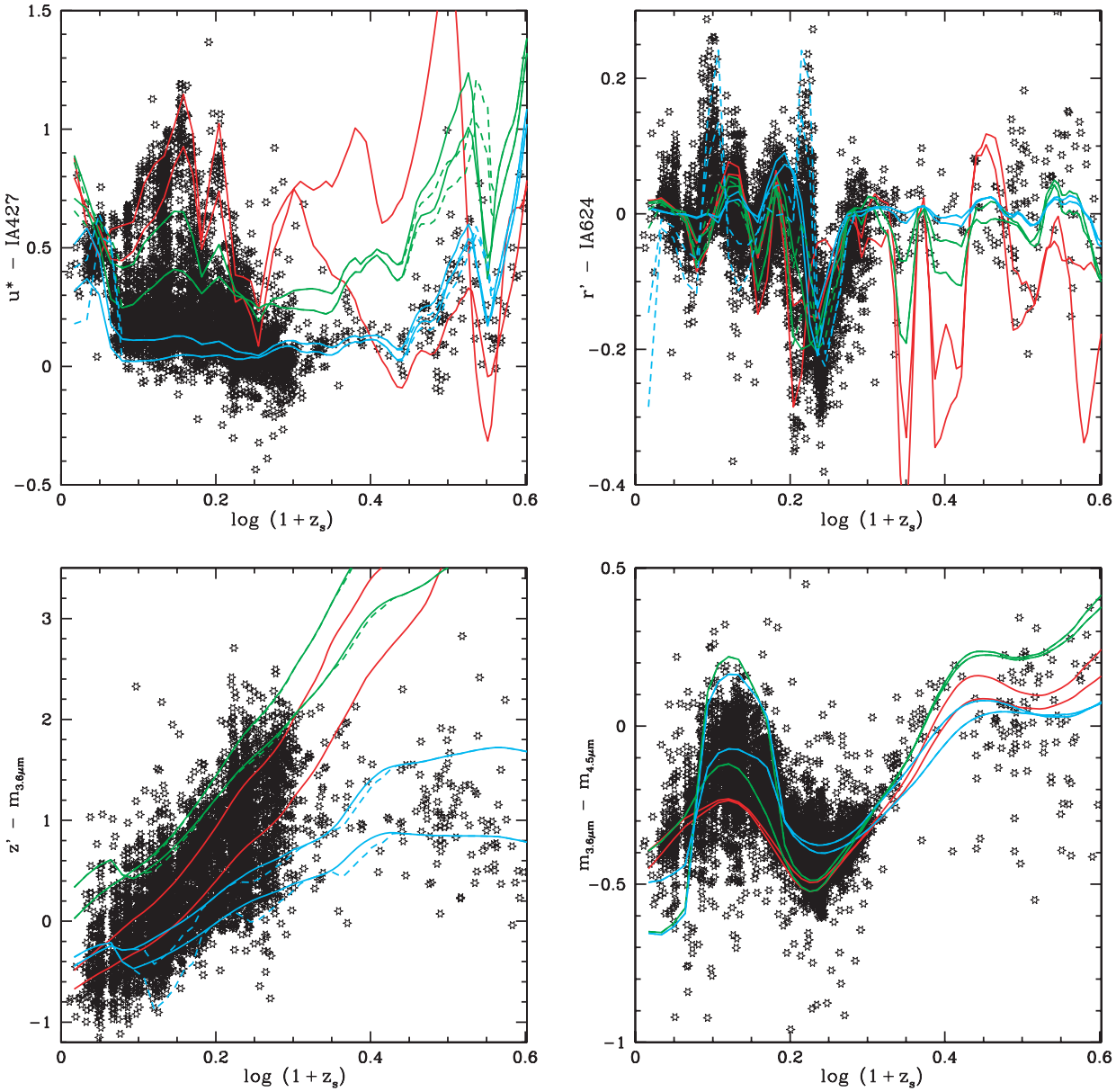


**Figure 2.** Observed colors and redshifts ($z_s$) for the spectroscopic sample galaxies (open stars). The solid lines are the predicted colors as a function of redshift for some SEDs of the library (red: elliptical; green: spiral from Polletta et al. 2007; cyan: BC03). The solid curves are the predicted colors without including emission lines (no reddening for the elliptical templates, $E(B-V) = 0.2$ for the late types) whereas the dashed curves are the same templates including the emission line fluxes (assuming $M_{\rm FUV} = -20$ in this example). The top right panel clearly shows that the emission lines can change the colors up to 0.4 mag.

(A color version of this figure is available in the online journal.)

where DM is the distance modulus, $F_{[\rm O\,II]}$ is expressed in units of $10^{-17}$ erg s$^{-1}$ cm$^2$, and $M_{\rm UV}$ is the dust-corrected UV(2300 Å) absolute magnitude.

Figure 3 shows the measured [O II] fluxes from VVDS (F. Lamareille et al. 2008, in preparation) and the relation (solid line) expected from Kennicutt (1998). We can perform this comparison only at $0.5 < z < 1.4$, when the [O II] line is observable in the VIMOS spectra. Figure 3 shows good correlation between the measured and predicted [O II] fluxes, with an rms dispersion of 0.2 dex. In the acknowledgment of this dispersion, we allow the intrinsic [O II] flux to vary by a factor of 2 in the templates with respect to the nominal flux predicted by Equation (1).

With our procedure, we can predict for each galaxy the [O II] flux at every redshift, template, and extinction combination. For the other emission lines, we adopt intrinsic, unextincted flux ratios of [O III/O II] = 0.36, [H$\beta$/O II] = 0.61, [H$\alpha$/O II] = 1.77, and [Ly$\alpha$/O II] = 2 (McCall et al. 1985; Moustakas et al. 2006; Mouhcine et al. 2005; Kennicutt 1998). When we apply an additional extinction to the template, we modify these ratios with the corresponding attenuation. Then, we sum the emission line fluxes to the template continuum before integrating through the filter transmission curves.

The effect of these emission lines on the modeled color–redshift relation is shown in Figure 2 for a galaxy at $M_{\rm UV} = -20$. The oscillations in the observed colors versus redshift are well reproduced by the models.

### 3.3. Systematic Offsets

The $\chi^2$ template-fitting method is meaningful only if the color–$z$ relation predicted from the templates is a good representation of the observed color–$z$ relation. Uncertainties in the

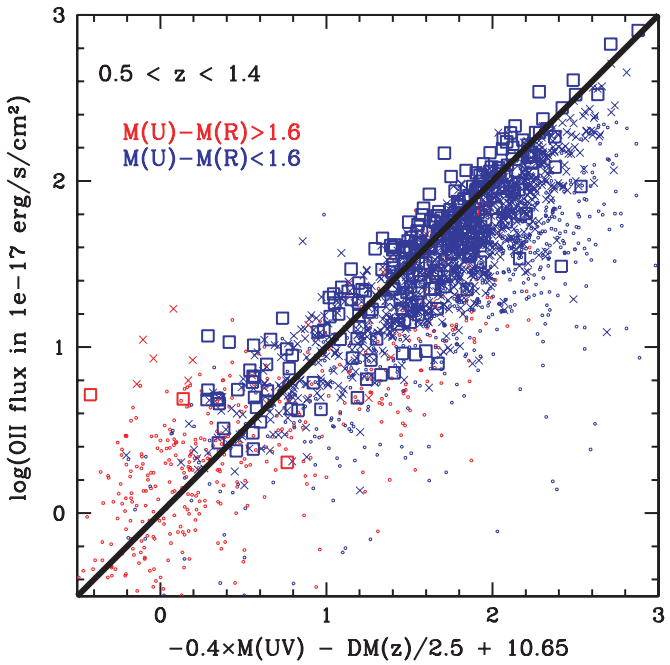


**Figure 3.** Relation between the [O II] flux and the absolute magnitudes in UV (2300 Å). The solid line corresponds to the relation obtained by applying the Kennicutt (1998) relations between $SFR_{O II}$ and $SFR_{UV}$ as used here to include emission line fluxes in the photo-z fitting (see Equation (1)) and the points are observed emission line fluxes from VVDS (F. Lamareille et al. 2008, in preparation). The UV luminosities and O II fluxes are corrected for dust extinction. The red and blue points are galaxies with $M_U - M_R > 1.6$ and $M_U - M_R < 1.6$, respectively. The larger symbols correspond to larger equivalent width.

(A color version of this figure is available in the online journal.)

zero-point offsets of photometric bands can lead to systematic shifts between the predicted color–$z$ relation and the observed colors of the spectroscopic sample.

To evaluate the zero-point errors, we use the spectroscopic sample and set the redshift to the spectro-z value. Then, we determine the best-fit template for each spectroscopic galaxy. For random, normally distributed uncertainties in the flux measurements, $\overline{\Delta F_f}$ should be $\sim 0$ (where $\overline{\Delta F_f}$ is the average difference between predicted and observed fluxes in the filter $f$). Instead, we initially find systematic offsets of $\overline{\Delta F_f}$ (as for earlier photo-z derivations, e.g., Brodwin et al. 2006; Ilbert et al. 2006; Mobasher et al. 2007). Such offsets are mainly due to (1) uncertainties in the absolute calibration of the photometric zero points and (2) uncertainties in the color modeling (filter transmission curves, incomplete set of templates, or an incorrect extinction curve). These systematic offsets were removed using the iterative procedure detailed in Ilbert et al. (2006). For each filter, $f$, we estimate the values $s_f$ which minimize $\overline{\Delta F_f}$. After having applied the corrections, $s_f$, in each band $f$, the systematic offsets derived in a second iteration can change. The values converge after three iterations and we adopted the systematic offsets listed in Table 1.

### 3.4. Extinction Law

Ilbert et al. (2006) adopted the dust-extinction law measured in the Small Magellanic Cloud (Prevot et al. 1984). However, considerable changes in the extinction curve are expected from galaxy to galaxy. Maraston et al. (2006) considered as a free parameter the different extinction curves of the "Hyperz" package (Bolzonella et al. 2000; e.g., Milky Way, Large and Small Magellanic Clouds, and Calzetti). In order to limit the risk of catastrophic failures, we adopt an intermediate approach here, using the most suitable extinction curve depending on the SED template.

For each galaxy of the zCOSMOS sample, we set the redshift to the spectro-z value. Then, we determine the best fit-template and the appropriate color excess $E(B-V)^{\rm best}$. In this fit, we assume an extinction curve $k(\lambda)$ ($= A(\lambda)/E(B-V)$). Since the extinction curves do not differ strongly at $\lambda > 3000$ Å (the blue and green curves in Figure 4), we fit the templates using only passbands with $\lambda > 3000(1+z)$ Å. With this procedure, the $E(B-V)^{\rm best}$ value does not depend significantly on the adopted extinction curve.

The extinction curves differ strongly at $\lambda < 3000$ Å. Therefore, we use the rest-frame observed SEDs at $\lambda_{\rm rest-frame} < 3000$ Å to discriminate between the different extinction curves. Using $m^{\rm obs}$ to represent the observed magnitude and $m^{\rm template}_{\rm uncor}$ to represent the predicted magnitude from the best-fit template (uncorrected for extinction), the extinction $A(\lambda)$ is given by $A(\lambda) = m^{\rm obs} - m^{\rm template}_{\rm uncor}$. Figure 4 shows the rest-frame $\left(m^{\rm obs} - m^{\rm template}_{\rm uncor}\right)/E(B-V)^{\rm best}$ for each flux measurement, i.e., the extinction curve $k(\lambda)$. These points are compared with the Calzetti et al. (2000) and the Prevot et al. (1984) extinction curves. We scaled the Prevot et al. (1984) curve to the same $A_V$ value as Calzetti et al. (2000) by applying a factor of 4.05/2.72, which is the ratio between the $R_V$ of the Calzetti and Prevot laws. The Small Magellanic Cloud extinction curve (Prevot et al. 1984) is well suited for galaxies redder than the starburst template SB3. For galaxies bluer than SB3, the Calzetti et al. (2000) extinction curve is found to be more appropriate (see Figure 4). For the IR sources which are strongly star forming, Caputi et al. (2008) show also that the Calzetti et al. (2000) extinction law is more appropriate. This result is not surprising since the Calzetti law was determined from observed starburst galaxies. A broad absorption excess at 2175 Å (UV bump) seems necessary to explain the UV flux in some starburst galaxies. The presence of this UV bump can be seen in a theoretical modeling of the Calzetti law (Fischera et al. 2003) and in the K20 sample of high-redshift galaxies at $1 < z < 2.5$ (Noll et al. 2007).

To summarize, we apply an additional extinction to the templates according to a grid $E(B-V) = 0, 0.05, 0.1, 0.15, 0.2, 0.25, 0.3, 0.4, 0.5$. We use the Prevot et al. (1984) extinction curve for the templates redder than SB3, and Calzetti et al. (2000) for the templates bluer than SB3. We allow an additional bump at 2175 Å for the Calzetti extinction law if it produces a smaller $\chi^2$. No reddening is allowed for galaxies redder than *Sb*.

### 3.5. $\chi^2$ Minimization

The photo-z is the redshift value which minimizes the merit function $\chi^2(z, T, A)$:

$$\chi^2 = \sum_{f=1}^{N_f} \left( \frac{F^f_{\rm obs} - A \times F^f_{\rm pred}(z,T)\ 10^{-0.4 s_f}}{\sigma^f_{\rm obs}} \right)^2, \qquad (2)$$

where $F^f_{\rm pred}(T,z)$ is the flux predicted for a template $T$ at redshift $z$. $F^f_{\rm obs}$ is the observed flux and $\sigma^f_{\rm obs}$ is the associated error. The index $f$ refers to each specific filter and $s_f$ is the zero-point offset listed in Table 1. The opacity of the intergalactic medium (Madau et al. 1996) is taken into account. The photo-z

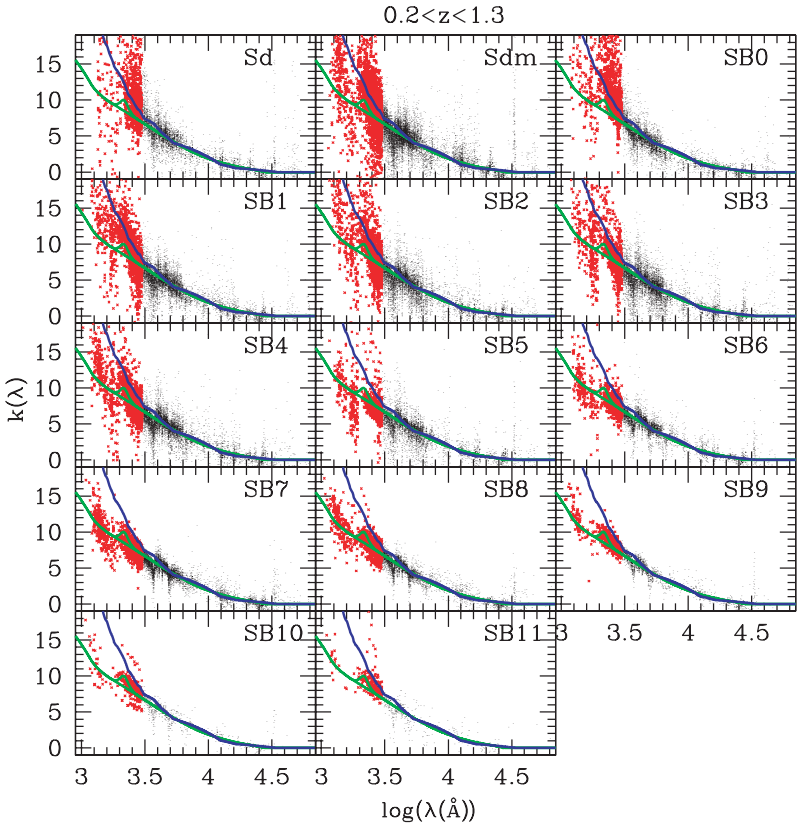


**Figure 4.** Attenuation by dust as a function of λ. The points are the extinction $A_i/(E_i(B-V))$ estimated from the galaxies with a spectro-z (see Section 3.4). The red points at $\lambda < 3000$ Å are not used to estimate $E_i(B-V)$. The Prevot et al. (1984) and Calzetti et al. (2000) extinction curves are shown with the blue and green solid lines, respectively. The Prevot et al. (1984) extinction law is rescaled to the same $A_V$ as the Calzetti law by applying a factor of 4.05/2.72. The extinction curve derived by Prevot et al. (1984) is used for the galaxies redder than SB3 and the Calzetti et al. (2000) extinction law for the galaxies bluer than SB3.

(A color version of this figure is available in the online journal.)

is estimated from the minimization of $\chi^2$ with respect to the free parameters, $z$, $T$, and the normalization factor $A$. The color excess $E(B-V)$ is included in the term $T$ (see Section 3.4). The grid spacing in redshift is $\delta z = 0.01$ and the final redshift is derived by parabolic interpolation of the redshift probability distribution. The redshift probability distribution function (PDFz) is derived directly from the $\chi^2(z)$ distribution:

$$P(z) \propto \exp\left(-\frac{\chi^2(z)-\chi^2_{\rm min}}{2}\right). \quad (3)$$

The minimum and maximum redshifts around the photo-z solution, corresponding to the $1\sigma$ errors, are estimated from the equation $\chi^2(z) = \chi^2_{\rm min} + 1$. As in Ilbert et al. (2006), we increased the SExtractor flux errors by a factor of 1.5. This factor does not shift the best-fit photo-z value but broadens the $\chi^2$ peak and derived redshift uncertainty.

### 3.6. Star/AGN/Galaxy Classification

For each object, $\chi^2$ is evaluated for both the galaxy templates and stellar SED templates (Chabrier et al. 2000; Bixler et al. 1991). If $\chi^2_{\rm gal} - \chi^2_{\rm star} > 0$, where $\chi^2_{\rm gal}$ and $\chi^2_{\rm star}$ are the minimum $\chi^2$ values obtained with the galaxy and stellar templates, respectively, the object is flagged as a possible star. Leauthaud et al. (2007) catalogued point-like sources in the COSMOS field using the peak surface brightness measured on the Advanced Camera for Surveys (ACS) images. The SED $\chi^2$ and morphological classification methods were found to be in excellent agreement—84% of the point-like sources at $i^+ < 24$ are classified as stars with the SED $\chi^2$ criterion mentioned above, while only 0.2% of the extended sources on the ACS images are misclassified as stars with the same $\chi^2$ criterion. As shown in Figure 5, the star sequence colors are well distinguished from the bulk of the galaxy population if the colors include a NIR band. NIR and mid-IR data are crucial to separate stars from galaxies. Therefore, we limit the $\chi^2$ star classification to $K < 24$ or $F_{3.6\,\mu\rm m} > 1$ $\mu$Jy. Two percent of the point-like sources with $i^+ < 24$ have $K > 24$ and $F_{3.6\,\mu\rm m} > 1$ $\mu$Jy. These objects, which are only 2% of the total population at $i^+ < 24$, could be stars not recognized as such by our SED $\chi^2$ classification.

AGN can be identified by their point-like X-ray emission. Most (∼90%) of the 1887 sources detected in *XMM*-COSMOS (Brusa et al. 2007) are dominated by an AGN. Their photo-z determinations require a different treatment: a correction for variability of the photometric data and the use of SED templates specifically tuned to AGN and their host galaxies. Accurate photo-z for the *XMM*-COSMOS sources are derived in a companion paper (Salvato et al. 2008). Due to the flux limit in *XMM*-COSMOS (Brusa et al. 2007), the moderately luminous ($\log(Lx) =$ 42–43 erg s$^{-1}$) and luminous ($\log(Lx) =$ 43–44 erg s$^{-1}$) AGN are not sampled by *XMM*-COSMOS at $z = 0.5$–$1.25$ and $z = 1.5$–$3$, respectively. Therefore, this population is not identified as AGN in the galaxy catalog.

## 4. PHOTO-Z ACCURACY

In this section, we assess the quality of the derived photo-z by two approaches: comparison with high-confidence spectro-z

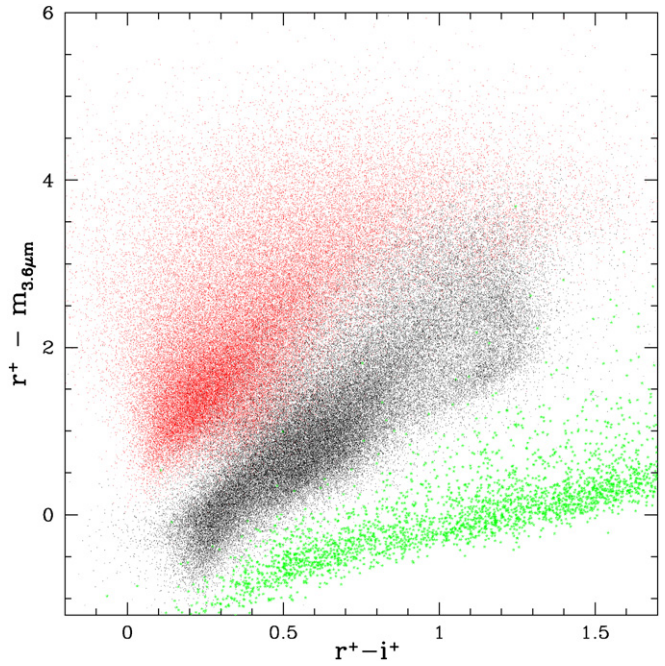


**Figure 5.** Color–color diagnostics for sources including stars and galaxies. Stars revealed by the $\chi^2$ classification are shown in green; the red and gray points are galaxies with $z_p > 1$ and $z_p < 1$, respectively.

(A color version of this figure is available in the online journal.)

and an analysis of the width of the redshift PDFz obtained from the $\chi^2$ fitting for the photo-z. The latter approach is justified by the excellent agreement of the $z_s$–$z_p$ distribution with the width of the PDFz for the spectroscopic sample.

### 4.1. Comparison of Photo-z and Spectro-z

We first assess the quality of the photo-z by comparison with the spectro-z. If $\Delta z = z_s - z_p$, we can estimate the redshift accuracy from $\sigma_{\Delta z/(1+z_s)}$ using the normalized median absolute deviation (NMAD; Hoaglin et al. 1983) defined as $1.48 \times \text{median}(|z_p - z_s|/(1 + z_s))$. The NMAD is directly comparable to other papers which directly quote the rms/(1+$z$). This dispersion estimate is robust with respect to catastrophic errors (i.e., objects with $|z_p - z_s|/(1 + z_s) > 0.15$). The percentage of catastrophic errors is denoted by $\eta$.

Figure 6 (left panel) shows the comparison between $z_p$ and $z_s$ for the zCOSMOS-bright sample selected at $i^+ < 22.5$. The spectro-z sample is selected only by apparent magnitude and is therefore representative of the entire $i^+ < 22.5$ population. We obtain an accuracy of $\sigma_{\Delta z/(1+z)} = 0.007$ at $i^+ < 22.5$ and the distribution of offsets $((z_p - z_s)/(1 + z_s))$ is well fit by a Gaussian with $\sigma = 0.007$ (Figure 6, right panel). The percentage of catastrophic failures is below 1%.

The zCOSMOS-faint sample (Figure 7, left panel) with a median apparent magnitude of $i^+_{\rm med} \sim 24$ provides a quality check for the photo-z at $1.5 < z < 3$ where the photo-z are expected to have a significantly higher uncertainty. The faint sample includes galaxies at $i^+ \sim 25$ and the Balmer break is shifted into the NIR where the filter set has gaps. At $1.5 < z < 3$, the accuracy is found to be $\sigma_{\Delta z/(1+z)} = 0.06$ with 20% catastrophic failures. The fraction of high-redshift galaxies ($z_s > 1.5$) for which a low-redshift photo-z ($z_p < 0.5$) was assigned is 7%, but this failure rate drops to 4% if the sample is restricted to galaxies detected at IRAC(3.6 $\mu$m) $> 1$ $\mu$Jy. The zCOSMOS-faint sample actually includes 54 galaxies with low spectro-z ($z_s < 0.5$); 53 out of the 54 galaxies ($> 98\%$) were assigned the correct photo-z low redshift. In summary, we conclude that, for the faint galaxies, the photo-z of low-redshift objects are still assigned correctly, while the failure rate for high-redshift objects is significantly reduced if the objects have good IRAC detections. Such result is expected since the photo-z are already including the same information present in high-z color selections such as $BzK$ (Daddi et al. 2004) or similar diagnostics using the IRAC bands (Figure 5) to isolate the good redshift range.

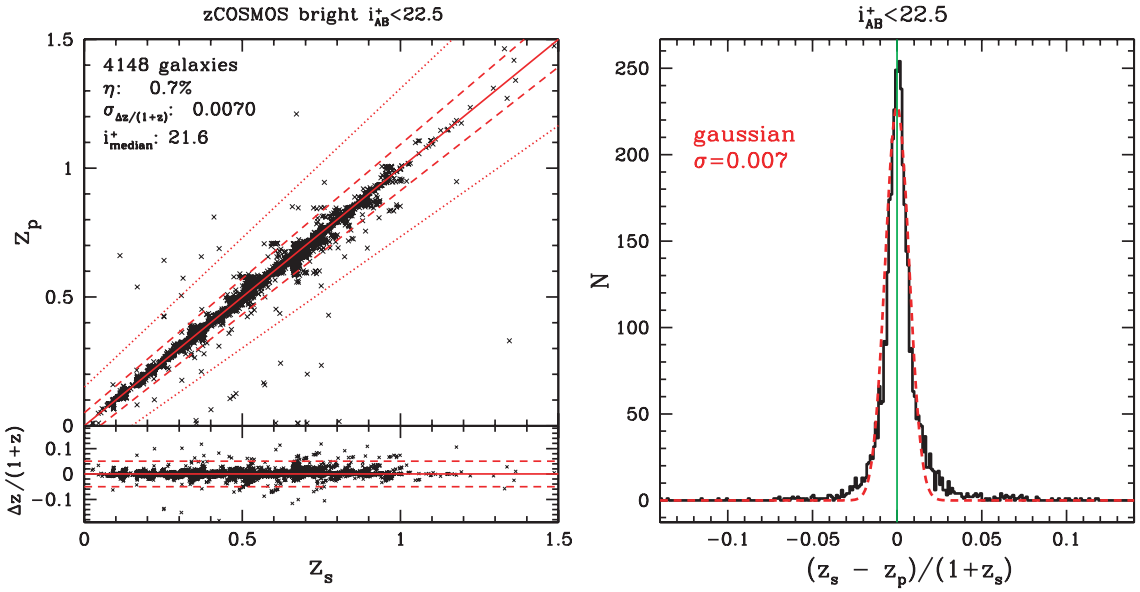


**Figure 6.** Left panel: comparison between $z_p$ and $z_s$ for the bright spectroscopic selected sample $17.5 \leqslant i^+_{\rm AB} \leqslant 22.5$ (zCOSMOS-bright; S. J. Lilly et al. 2008, in preparation). The dotted and dashed lines are for $z_p = z_s \pm 0.15(1+z_s)$ and $z_p = z_s \pm 0.05(1+z_s)$, respectively. The $1\sigma$ dispersion, the fraction of catastrophic failures and the median apparent magnitude are listed in the top-left corner of the left panel. Right panel: $\Delta z/(1 + z_s)$ distribution. The dashed line is a Gaussian distribution with $\sigma = 0.007$.

(A color version of this figure is available in the online journal.)

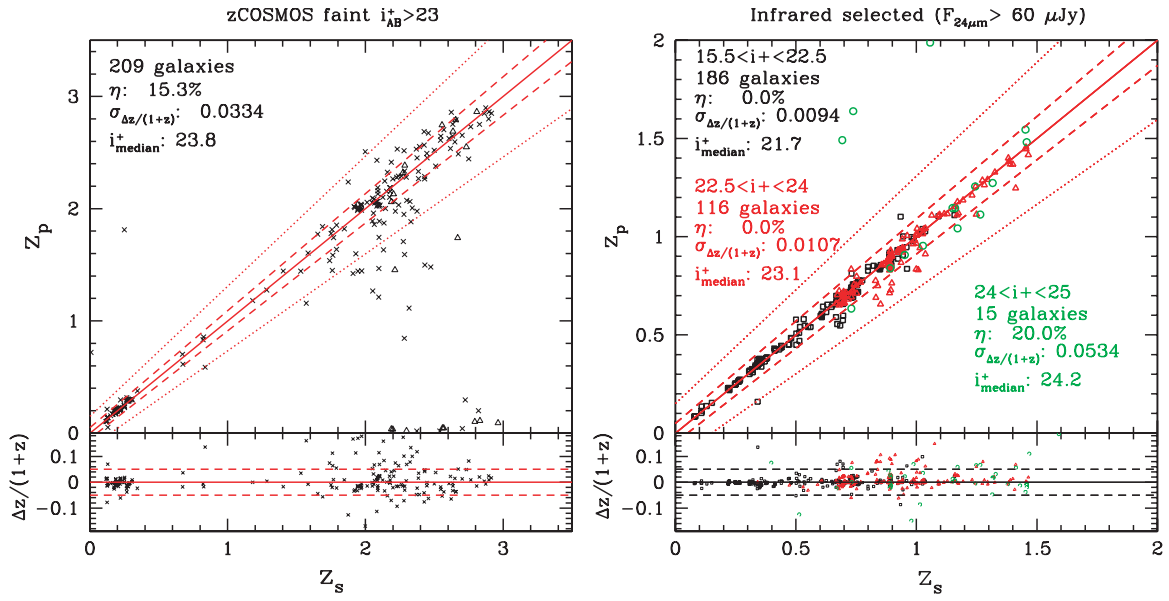


**Figure 7.** Comparison between $z_p$ and $z_s$. Left panel: zCOSMOS-faint sample (S. J. Lilly et al. 2008, in preparation). The open triangles are objects with a secondary peak in the redshift PDFz. Right panel: IR-selected sample (J. Kartaltepe et al. 2008, in preparation) split into a bright sample $i^+ < 22.5$ (black), a faint sample $22.5 < i^+ < 24$ (red), and a very faint sample $24 < i^+ < 25$ (green).

(A color version of this figure is available in the online journal.)

The zCOSMOS-bright and zCOSMOS-faint samples do not probe $0.2 < z < 1.5$ at $i^+ > 22.5$. Here, we use as a comparison sample the MIPS-spectro-z (J. Kartaltepe et al. 2008, in preparation). In Figure 7 (right panel), we split the MIPS-spectro-z sample into bright ($i^+ < 22.5$), faint ($22.5 < i^+ < 24$), and very faint samples ($24 < i^+ < 25$). For the bright subsample, the dispersion of the MIPS-selected galaxies is $\sigma_{\Delta z/(1+z_s)} = 0.009$, only slightly greater than that of the optically selected sample at $i^+ < 22.5$. For the faint subsample (median apparent magnitude $i^+ \sim 23.1$), $\sigma_{\Delta z/(1+z_s)} = 0.011$, i.e. slightly worse than for the brighter optically selected objects. For the very faint subsample, the accuracy is degraded to $\sigma_{\Delta z/(1+z_s)} = 0.053$ with a catastrophic failures rate of 20%. This degradation is due to decreasing signal-to-noise photometry for faint objects and could be amplified by the IR selection, which picks up more heavily obscured galaxies and higher redshift galaxies (e.g., Figure 4 of Le Floc'h et al. 2005).

### *4.2. Accuracy Derived from the Photo-z PDFz*

Since evaluation of the photo-z accuracy from the comparison with spectro-z is limited to specific ranges of magnitude and redshift, we use the $1\sigma$ uncertainty in the derived photo-z probability distribution to extend the uncertainty estimates over the full magnitude/redshift space.

The reliability of the $1\sigma$ uncertainty estimate for the photo-z as derived from the PDFz (see Section 3.5) can be checked by comparing this uncertainty with that derived directly from the photo-z–spectro-z offsets for the spectroscopic sample. Figure 8 shows the cumulative distribution of these offsets normalized by the $1\sigma$ uncertainty in the probability function for the zCOSMOS-bright sample (the ratio $|z_p - z_s|/(1\sigma$ error) is lower than 1 if the measured offset $z_p - z_s$ is lower than the $1\sigma$ uncertainty). Sixty-five percent of the $z_p$ are within the $1\sigma$ error bars, whereas the expected fraction is 68%. We therefore conclude that the $1\sigma$ uncertainties in the probability function as derived here provide a robust assessment of the accuracy in $z_p$.

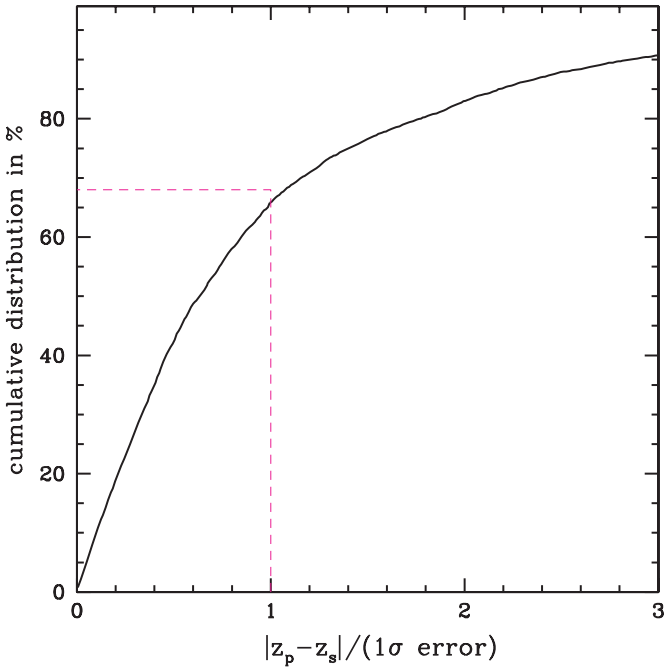


**Figure 8.** Cumulative distribution of the ratio $|z_p - z_s|/(1\sigma$ error). Sixty-five percent of the photo-z have a spectro-z solution encompassed within the $1\sigma$ error, close to the expected value of 68% (magenta dashed line).

(A color version of this figure is available in the online journal.)

Figure 9 shows the $1\sigma$ negative and positive uncertainties derived from the probability function as a function of redshift and apparent magnitude. Two clear conclusions emerge: the accuracy is inevitably degraded for fainter galaxies at all redshifts and the photo-z have significantly higher uncertainty at $z \gtrsim 1.25$.

From $z > 0$ out to $z = 1.25$, the $1\sigma$ errors do not depend significantly on the redshift, with $\sigma_{\Delta z} \lesssim 0.02$ at $i^+ < 24$ (note that we dropped out the division of $\sigma$ by $(1 + z)$ in

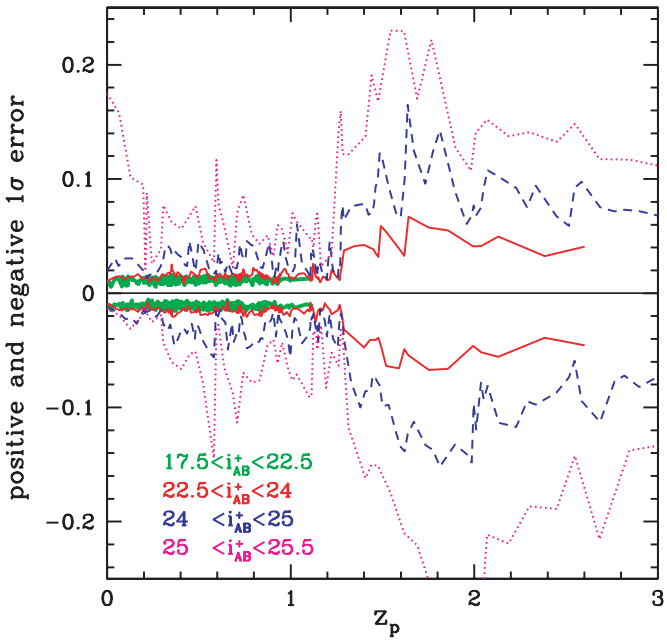


**Figure 9.** $1\sigma$ uncertainty for the $z_p$ estimate as a function of redshift in different apparent magnitude bin. Each value is computed with 50 galaxies per bin. The thick solid green lines, the solid red line, the dashed blue lines, and the dotted magenta lines are for $i^+ < 22.5$, $22.5 < i^+ < 24$, $24 < i^+ < 25$, and $25 < i^+ < 25.5$, respectively.

(A color version of this figure is available in the online journal.)

this analysis). To first order, the photo-z are accurate when the wavelengths of the Balmer and/or Lyman breaks are well constrained. Therefore, the wavelength coverage of the filter set and the photometry sensitivities determine the photo-z accuracy as a function of redshift. The COSMOS photometry coverage is continuous and dense in the optical from the $u^*$ band ($\lambda_{\rm eff} \sim 3911$ Å) to the $z^+$ band ($\lambda_{\rm eff} \sim 9021$ Å). The average wavelength spacing between consecutive filters is also only 230 Å. The Balmer break at redshift $z = 0$ out to $z = 1.25$ is always at $\lambda < 9000$ Å, thus the high accuracy in this redshift range.

The accuracy degrades at $z > 1.25$, where the 4000 Å Balmer break goes out of the $z^+$ band; at $z \sim 1.8$ it is a factor of 3 larger than at $z \sim 1.25$ ($\sigma_{\Delta z} \sim 0.14$ for $i^+ \sim 24$). The lack of coverage between the $z'$ and the $J$ band accounts for the discontinuous increase in uncertainty at $z > 1.25$ since the Balmer break cannot be located with precision. At $z > 1.5$, the estimated error from the photo-z–spectro-z comparison is $\sigma_{\Delta z} = 0.19$ (see Section 4.1; $\sigma_{\Delta z/(1+z_s)} = 0.06$ at the median redshift $z \sim 2.2$). This accuracy is $\sim$1.4 higher than that estimated from the $1\sigma$ uncertainty ($\sigma_{\Delta z} \sim 0.14$ at $i^+ \sim 24$). Errors due to bias in photo-z will not be recovered from the PDFz, which could explain this difference. At $z > 1.25$, all the optical filters, which are about 80% of all the used filters, are sampling the rest-frame UV at $\lambda < 3500$ Å. Uncertainties in the adopted extinction law have considerable impact on the UV slope and could introduce small biases in the estimate of the photo-z.

At $z > 2.5$, the accuracy improves again ($\sigma_{\Delta z} \lesssim 0.1$ for $24 < i^+ < 25$) when the 4000 Å Balmer break enters in the $J$ band ($z \sim 2$) and the UV light shortward of $L_\alpha$ enters the $u^*$ band ($z \sim 2.3$).

### 4.3. Importance of Zero-Point Offsets and Emission Lines

The major improvements in the technique implemented here are the carefully iterative evaluation of the photometric zero-point offsets for all bands and the allowance for a range of emission line contributions to the fluxes of template SEDs.

The left panel of Figure 10 shows the comparison between $z_p$ and $z_s$ computed without correction of the systematic band offsets (see Section 3.3) and without including the emission

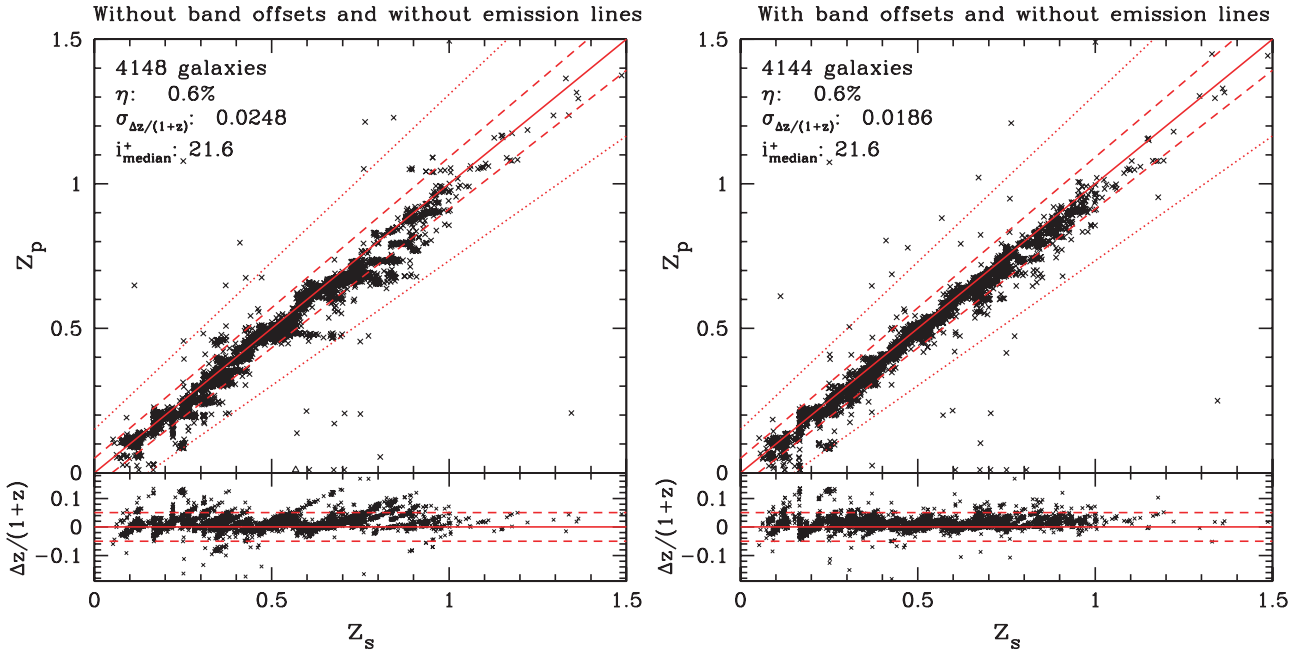


**Figure 10.** Comparison between $z_p$ and $z_s$ at different steps of the method. The comparison is done for the zCOSMOS-bright sample selected at $17.5 \leqslant i^+ \leqslant 22.5$. The left panel shows the photo-z computed with a standard $\chi^2$ method (no emission lines contributions and without calibration of the band offsets). The right panel shows $z_p$ computed with the calibration of the band offsets, but without including emission lines in the templates. Including emission lines improves the accuracy by a factor of $\sim$2.5.

(A color version of this figure is available in the online journal.)

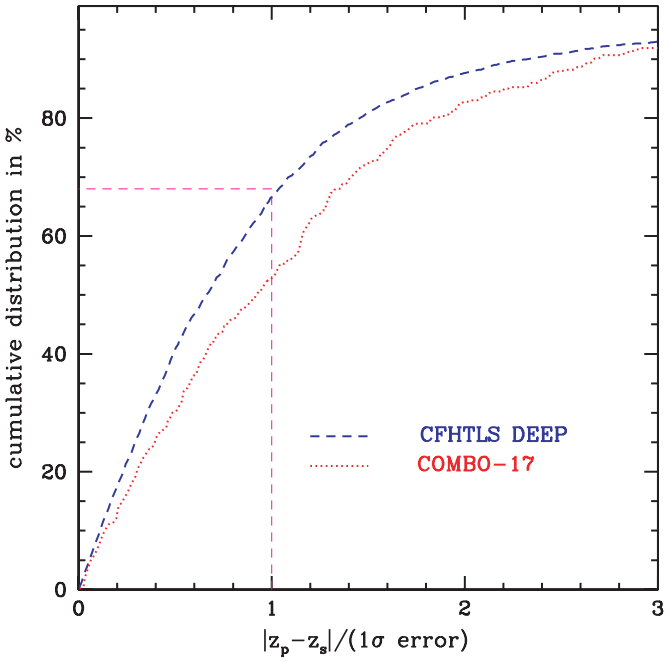


**Figure 11.** Same as Figure 8 for the CFHTLS-DEEP survey (Ilbert et al. 2006) and the COMBO-17 survey (Wolf et al. 2004).

(A color version of this figure is available in the online journal.)

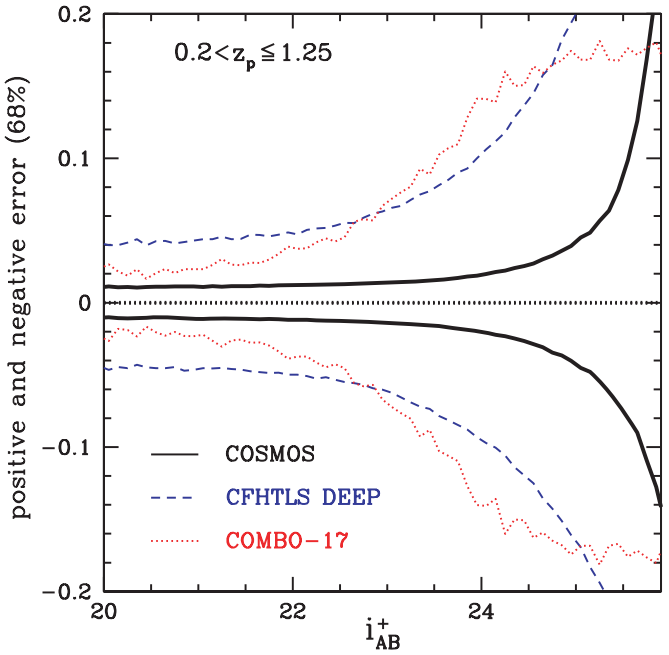


**Figure 12.** 1$\sigma$ error for the $z_p$ estimate as a function of the apparent magnitude in the redshift range $0.2 < z < 1.25$. The 1$\sigma$ errors have been rescaled by a factor of 1.2 for the COMBO-17 survey (Wolf et al. 2004; see text and Figure 11).

(A color version of this figure is available in the online journal.)

lines (see Section 3.2). Some systematic biases (horizontal and vertical stripes in Figure 10) greater than $\delta_z \sim 0.1$ are clearly seen in the photo-z estimate. For example, galaxies with $z_s \sim 0.8$ are often shifted to $z_z \sim 0.7$. With the iterative calibration of the band offsets turned on (the right panel of Figure 10), these biases are limited to $\delta_z < 0.05$. This clearly demonstrates the importance of zero-point calibration to reduce the photo-z bias (as already shown by Brodwin et al. 2006 and Ilbert et al. 2006).

The right panel of Figure 10 shows the comparison between $z_p$ and $z_s$ without including the emission lines (see Section 3.2). The accuracy is $\sigma_{\Delta z/(1+z_s)} \sim 0.02$. When the emission lines are included in the templates, the accuracy is improved by a factor of 2.5 ($\sigma_{\Delta z/(1+z_s)} = 0.007$; the left panel of Figure 6). Therefore, including emission lines in the SEDs is crucial, especially when the medium bands are used to measure $z_p$.

## 5. DISCUSSION

### 5.1. Comparison With Other Surveys

We now compare the accuracy of the COSMOS-30 photo-z (this work) with those obtained previously for COMBO-17 (Wolf et al. 2004) and CFHTLS-DEEP (Ilbert et al. 2006). The accuracies can be compared as a function of apparent magnitude using the 1$\sigma$ measured uncertainties in the photo-z probabilities. Once again, we check also the validity of the 1$\sigma$ uncertainties for other surveys following the method described in Section 4.2. For the COMBO-17 and CFHTLS photo-z, we use the spectro-z from the VIMOS-VLT Deep Survey (Le Fèvre et al. 2004, 2005). Figure 11 shows that about 53% and 67% of the values for $z_s$ are included inside the 1$\sigma$ uncertainties for COMBO-17 and CFHTLS-DEEP survey, respectively. The 1$\sigma$ errors for $z_p$ in COMBO-17 are rescaled by ~1.2 to obtain 68% of the $z_s$ within the 1$\sigma$ error (this rescale is small and changes nothing in our conclusions).

Figure 12 shows the redshift dependence of the 1$\sigma$ uncertainties in photo-z as a function of magnitude for $0.2 < z < 1.25$. The $z_p$ for the CFHTLS-DEEP were derived from five broadbands ($u^*$, $g'$, $r'$, $i'$, $z'$). The accuracy of the COSMOS photo-z is improved by a factor of 3 when compared to CFHTLS-DEEP. This improvement is largely due to the 12 medium bands in this redshift range (NIR data have a real impact only at $z > 1.25$). We checked this by deriving photo-z without the 12 medium bands, obtaining an accuracy of $\sigma_{\Delta z/(1+z_s)} = 0.03$ at $i^+ < 22.5$ (similar to the COSMOS release of Mobasher et al. 2007 using eight broadbands $u^*$, $B_J$, $V_J$, $g^+$, $r^+$, $i^+$, $z^+$, and $K_S$). COMBO-17 includes 12 medium bands in addition to the five broadbands and Wolf et al. (2004) achieved an accuracy of $\sigma_{\Delta z/(1+z)} = 0.02$ at $i^+ \sim 21.5$. The accuracies of COMBO-17 photo-z are intermediate between those of COSMOS-30 and CFHTLS for $i^+_{AB} < 22.5$ but become larger than the CFHTLS accuracies at fainter magnitudes, because the COMBO-17 data are about 1.5 mag shallower than the CFHTLS data. Since only secure photo-z (one solution) have been kept in the COMBO-17 catalog, it explains the flattening of the error bars at $i^+_{AB} > 24$.

### 5.2. Redshift Distribution of Galaxies

Figure 13 shows the galaxy redshift distribution per deg$^2$ from the COSMOS and CFHTLS surveys (for $21.5 < i^+_{\rm auto} < 24.5$). Although the surveys are largely independent and the photo-z are computed with different codes, the overall agreement in the redshift distributions is excellent. The agreement is particularly good between COSMOS and CFHTLS-D2 which covers 1 deg$^2$ within the COSMOS field.

The density of galaxies at $z > 1.5$ in the CFHTLS fields is of crucial interest for weak lensing analysis (Benjamin et al. 2007). The CFHTLS redshift distribution presents a bump at $z \sim 3$, but this excess could be due to misidentifications between the $z < 0.4$ and $z > 1.5$ photo-z (L. van Waerbeke 2008, in preparation) when no NIR data are available (as is the case for CFHTLS). The COSMOS photo-z are computed

**Table 2**
Galaxy Redshift Distribution per deg$^2$

| Mag Range | $a$ | $b$ | $c$ | $A$ | Average $z$ | Median $z$ |
|---|---|---|---|---|---|---|
| $22.0 < i^+_{\rm auto} < 22.5$ | 0.497 ± 0.019 | 12.643 ± 0.409 | 0.381 ± 0.016 | 4068.19 | 0.66 | 0.66 |
| $22.5 < i^+_{\rm auto} < 23.0$ | 0.448 ± 0.016 | 9.251 ± 0.218 | 0.742 ± 0.030 | 9151.98 | 0.76 | 0.72 |
| $23.0 < i^+_{\rm auto} < 23.5$ | 0.372 ± 0.012 | 6.736 ± 0.094 | 1.392 ± 0.055 | 18232.24 | 0.90 | 0.82 |
| $23.5 < i^+_{\rm auto} < 24.0$ | 0.273 ± 0.008 | 5.281 ± 0.039 | 2.614 ± 0.096 | 35508.58 | 1.05 | 0.92 |
| $24.0 < i^+_{\rm auto} < 24.5$ | 0.201 ± 0.005 | 4.494 ± 0.024 | 3.932 ± 0.134 | 60306.30 | 1.18 | 1.00 |
| $24.5 < i^+_{\rm auto} < 25.0$ | 0.126 ± 0.003 | 4.146 ± 0.021 | 5.925 ± 0.191 | 103340.04 | 1.25 | 1.06 |

**Note.** The parameters $a$, $b$, $c$, and $A$ of the Equation (4) function (Fu et al. 2008) are given per apparent bin.

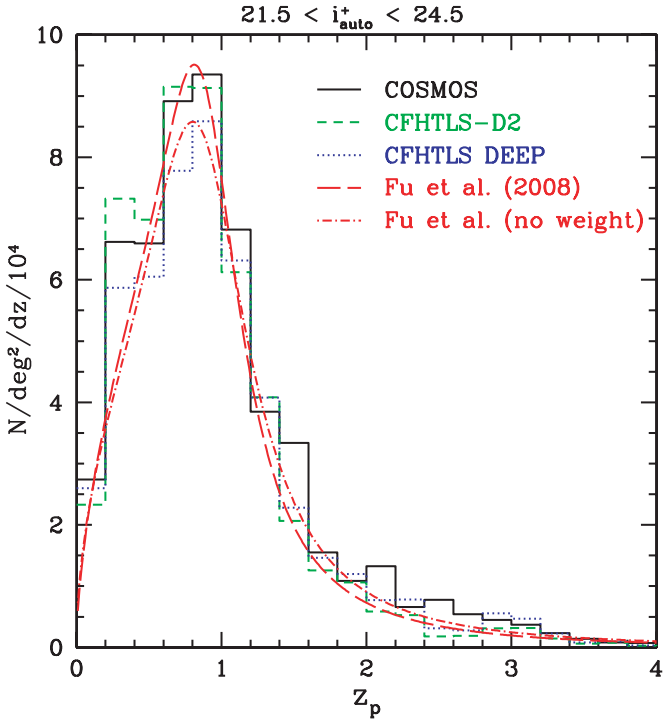


**Figure 13.** Redshift distribution from the 2-deg$^2$ COSMOS survey (black solid line), from the 1-deg$^2$ CFHTLS-D2 field (green dashed line), from the 4-deg$^2$ CFHTLS-DEEP fields (blue dotted line, including also D2). CFHTLS-D2 covers 1 deg$^2$ within the COSMOS field. The red long dashed line is the redshift distribution obtained by Fu et al. (2008) who fit the CFHTLS-DEEP photo-z in the magnitude bin $21.5 < i^+ < 24.5$ and the dashed-dotted line is obtained without the weight applied for the CFHTLS weak lensing selection (J. Coupon 2008, private communication).

(A color version of this figure is available in the online journal.)

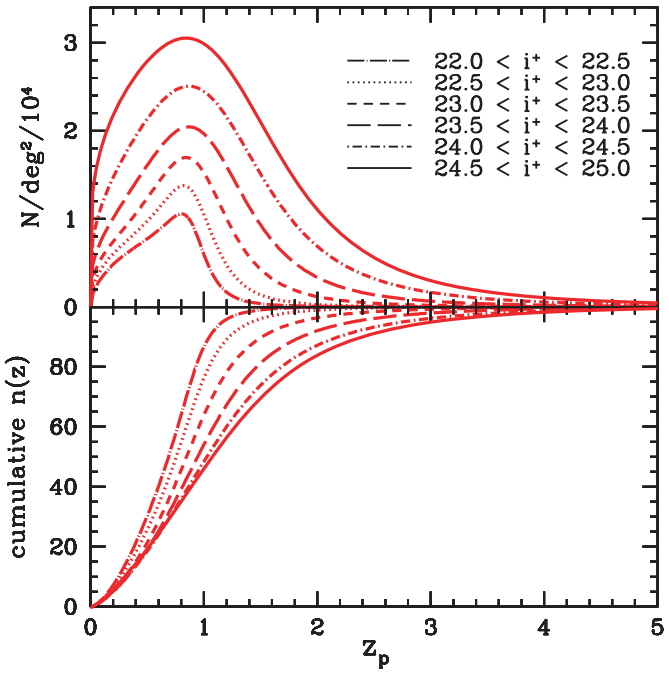


**Figure 14.** Top panel: evolution of the redshift distribution as a function of $i^+$ magnitude in the COSMOS field. We use the parametrization of Fu et al. (2008) in different redshift bins. Bottom panel: cumulative redshift distribution.

(A color version of this figure is available in the online journal.)

with NIR data and such catastrophic failures are limited (see Section 4.1). Figure 13 shows that this bump seems created by a deficit of galaxies at $2.5 < z < 3$, by comparing CFHTLS-D2 and COSMOS.

Fu et al. (2008) used the CFHTLS photo-z distribution to estimate the matter density parameter $\Omega_{\rm m}$ and the amplitude of the matter power spectrum $\sigma_8$. The redshift distribution from Fu et al. (2008) at $21.5 < i^+ < 24.5$ and $z < 2.5$ is over-plotted in Figure 13 with and without (J. Coupon 2008, private communication) the weight applied for the weak lensing selection (dashed and dashed-dot lines, respectively). Given the 20% variation expected from cosmic variance (Ilbert et al. 2006), it is in excellent agreement with the COSMOS-30 redshift distribution. This agreement suggests that the derivation of $\sigma_8(\Omega_{\rm m}/0.25)^{0.64} = 0.785 \pm 0.043$ by Fu et al. (2008) is not suffering from biases due to the photo-z or significant cosmic variance.

The COSMOS-30 redshift distribution can be fit with a parametrization similar to that used by Fu et al. (2008):

$$n(z) = A\frac{(z^a + z^{ab})}{(z^b + c)}, \quad (4)$$

where $A$ is the normalization factor and $a$, $b$, and $c$ are free parameters. The best-fit parameters $a$, $b$, and $c$ are given in Table 2, as well as the median redshifts. Figure 14 shows the best-fit redshift distribution per apparent magnitude bin. As expected, the median redshift increases at fainter apparent magnitude, ranging from $z_{\rm m} = 0.66$ at $22 < i^+ < 22.5$ to $z_{\rm m} = 1.06$ at $24.5 < i^+ < 25$.

## 6. SUMMARY

This paper presents a new version of the photo-z catalog for the 2-deg$^2$ COSMOS survey computed with new ground-based NIR data, deeper IRAC data, and a new set of 12 medium bands from the Subaru Telescope. The COSMOS photometry now includes a total of 30 filters—from the UV (*GALEX*) to the mid-IR (*Spitzer*-IRAC). The photo-z catalog derived here contains 607,617 sources at $i^+ < 26$. The 1887 *XMM*-COSMOS sources (mainly AGN) are not included in this catalog; their photo-z are

**Table 3**
Redshift Accuracies Estimated from the Comparison Between Photo-z and Spectro-z

| Sample | | $N$ | Median $z_s$ | Median $i^+$ | $\sigma_{\Delta z/(1+z_s)}$ | $\eta$ (%) |
|---|---|---|---|---|---|---|
| zCOSMOS bright | $17.5 < i^+ < 22.5$ | 4146 | 0.48 | 21.6 | 0.007 | 0.7 |
| zCOSMOS faint | $1.5 < z_s < 3$ | 147 | 2.20 | 24.0 | 0.054 | 20.4 |
| MIPS bright | $17.5 < i^+ < 22.5$ | 186 | 0.68 | 21.7 | 0.009 | 0.0 |
| MIPS faint | $22.5 < i^+ < 24.0$ | 116 | 0.90 | 23.1 | 0.011 | 0.0 |
| MIPS very faint | $24.0 < i^+ < 25.0$ | 15 | 1.15 | 24.2 | 0.053 | 20.0 |

derived by Salvato et al. (2008) with similarly good accuracy using a set of templates for composite AGN/galaxies.

The galaxy photo-z were tested and improved using spectro-z samples from the zCOSMOS and Keck surveys. Biases in the photo-z were removed by iterative calibration of the photometric band zero points. As suggested by the data, two different dust-extinction laws were applied specific to the different SED templates. A new method to take into account the emission lines was implemented using relations between the UV continuum and the emission line fluxes associated with star-formation activity. The allowance for emission lines decreased the photo-z dispersion by a factor of 2.5.

Based on a comparison between our new values for $z_p$ and 4148 measured values of $z_s$ from zCOSMOS, we estimate an accuracy of $\sigma_{\Delta z/(1+z_s)} = 0.007$ for the galaxies brighter than $i^+ = 22.5$. The accuracies measured with the various spectroscopic samples are summarized in Table 3. We extrapolate this result to fainter magnitudes using the $1\sigma$ uncertainties in the photo-z probability functions. This is found to provide reliable uncertainty estimates for the photo-z technique developed here since these uncertainties agree with the dispersion in the offsets of photo-z from spectro-z for the spectroscopic sample. At $z < 1.25$, we estimate a photo-z accuracy of $\sigma_{\Delta z} = 0.02$, 0.04, 0.07 for $i^+ \sim 24$, $i^+ \sim 25$, $i^+ \sim 25.5$, respectively. The accuracy is strongly degraded at $i^+ > 25.5$ and the exploitation of the COSMOS-30 photo-z at fainter magnitudes should be done carefully. The accuracy is 3–5 times better than the photo-z determined for the CFHTLS-DEEP (Ilbert et al. 2006) and the previous COSMOS photo-z release (Mobasher et al. 2007), and 2 times better than the accuracy of the photo-z determined for COMBO-17 at $i^+ < 23$ (Wolf et al. 2004). Deep NIR ($J$, $K$) and IRAC data were essential to keep the catastrophic failures low at $z > 1.25$. We note that the accuracy of the COSMOS photo-z could soon be further improved at $z > 1.25$ with the addition of new data currently being obtained in the $Y$ band (UKIRT), $H$ band (CFHT), and the ULTRA-VISTA survey.

Our photo-z catalog contains 607,617 sources at $i^+ < 26$. The accurate photo-z derived here for this extremely large sample of galaxies are crucial to scientifically exploit the full legacy value of the multi-λ data sets in the COSMOS field (*HST*-ACS, *Spitzer*, *GALEX*, VLA, *XMM*, and *Chandra*).

We gratefully acknowledge the contributions of the entire COSMOS collaboration consisting of more than 100 scientists. The *HST* COSMOS program was supported through NASA grant HST-GO-09822. More information on the COSMOS survey is available at Web site http://www.astro.caltech.edu/cosmos. We also greatly appreciate the hospitality provided by the Aspen Center for Physics where this manuscript was completed.

This article is based on observations with the NASA/ESA *Hubble Space Telescope*, obtained at the Space Telescope Science Institute, which is operated by AURA Inc., under NASA contract NAS 5-26555. It is also based on observations made with the *Spitzer Space Telescope*, which is operated by the Jet Propulsion Laboratory, California Institute of Technology, under NASA contract 1407. The research is also based on data collected at: the Subaru Telescope, which is operated by the National Astronomical Observatory of Japan; the *XMM-Newton*, an ESA science mission with instruments and contributions directly funded by ESA Member States and NASA; the European Southern Observatory under Large Program 175.A-0839, Chile; Kitt Peak National Observatory, Cerro Tololo Inter-American Observatory, and the National Optical Astronomy Observatory, which are operated by the Association of Universities for Research in Astronomy, Inc. (AURA) under cooperative agreement with the National Science Foundation; and the Canada–France–Hawaii Telescope (CFHT) with MegaPrime/MegaCam operated as a joint project by the CFHT Corporation, CEA/DAPNIA, the NRC and CADC of Canada, the CNRS of France, TERAPIX, and the University of Hawaii.

## REFERENCES

Arnouts, S., et al. 1999, MNRAS, 310, 540
Arnouts, S., et al. 2007, A&A, 476, 137
Ball, N. M., Loveday, J., Fukugita, M., Nakamura, O., Okamura, S., Brinkmann, J., & Brunner, R. J. 2004, MNRAS, 348, 1038
Baum, W. A. 1962, in IAU Symp. 15, Problems of Extra-Galactic Research, ed. G. C. McVittie (New York: MacMillan), 390
Benjamin, J., et al. 2007, MNRAS, 381, 702
Bertin, E., & Arnouts, S. 1996, A&AS, 117, 393
Bixler, J. V., Bowyer, S., & Laget, M. 1991, A&A, 250, 370
Bolzonella, M., Miralles, J.-M., & Pelló, R. 2000, A&A, 363, 476
Boulade, O., et al. 2003, in Proc. SPIE, 4841, Instrument Design and Performance for Optical/Infrared Ground-based Telescopes, ed. M. Iye & A. F. M. Moorwood (Bellingham, WA: SPIE), 72
Brodwin, M., et al. 2006, ApJS, 162, 20
Brusa, M., et al. 2007, ApJS, 172, 353
Bruzual, G., & Charlot, S. 2003, MNRAS, 344, 1000
Budavári, T., Szalay, A. S., Connolly, A. J., Csabai, I., & Dickinson, M. 2000, AJ, 120, 1588
Calzetti, D., et al. 2000, ApJ, 533, 682
Capak, P., et al. 2007, ApJS, 172, 99
Caputi, K. I., McLure, R. J., Dunlop, J. S., Cirasuolo, M., & Schael, A. M. 2006, MNRAS, 366, 609
Caputi, K. I., et al. 2008, ApJ, 680, 939
Chabrier, G., Baraffe, I., Allard, F., & Hauschildt, P. 2000, ApJ, 542, 464
Coleman, G. D., Wu, C.-C., & Weedman, D. W. 1980, ApJS, 43, 393
Collister, A. A., & Lahav, O. 2004, PASP, 116, 345
Daddi, E., Cimatti, A., Renzini, A., Fontana, A., Mignoli, M., Pozzetti, L., Tozzi, P., & Zamorani, G. 2004, ApJ, 617, 746
Feldmann, R., et al. 2006, MNRAS, 372, 565
Fernández-Soto, A., Lanzetta, K. M., & Yahil, A. 1999, ApJ, 513, 34
Fischera, J., Dopita, M. A., & Sutherland, R. S. 2003, ApJ, 599, L21
Fontana, A., et al. 2000, AJ, 120, 2206
Fu, L., et al. 2008, A&A, 479, 9
Gabasch, A., et al. 2004, A&A, 421, 41
Guillaume, M., Llebaria, A., Aymeric, D., Arnouts, S., & Milliard, B. 2006, in Proc. SPIE, 6064, Image Processing: Algorithms and Systems, Neural Networks, and Machine Learning, ed. E. R. Dougherty et al. (Bellingham, WA: SPIE), 332
Heinis, S., et al. 2007, ApJS, 173, 503
Hoaglin, D. C., Mosteller, F., & Tukey, J. W. 1983, Understanding Robust and Exploratory Data Analysis (New York: Wiley)
Ilbert, O., et al. 2006, A&A, 457, 841
Kennicutt, R. C. 1998, ARA&A, 36, 189
Leauthaud, A., et al. 2007, ApJS, 172, 219
Le Fèvre, O., et al. 2004, A&A, 428, 1043

Le Fèvre, O., et al. 2005, A&A, 439, 845
Le Floc'h, E., et al. 2005, ApJ, 632, 169
Lilly, S. J., et al. 2007, ApJS, 172, 70
Lonsdale, C. J., et al. 2003, PASP, 115, 897
Madau, P., et al. 1996, MNRAS, 283, 1388
Maraston, C., et al. 2006, ApJ, 652, 85
Mazure, A., et al. 2007, A&A, 467, 49
McCall, M. L., Rybski, P. M., & Shields, G. A. 1985, ApJS, 57, 1
McCracken, H. J., Ilbert, O., & Mellier, Y. 2007, A&A, 479, 431
Mobasher, B., et al. 2007, ApJS, 172, 117
Mouhcine, M., Lewis, I., Jones, B., Lamareille, F., Maddox, S. J., & Contini, T. 2005, MNRAS, 362, 1143
Moustakas, J., Kennicutt, R. C., & Tremonti, C. A. 2006, ApJ, 642, 775
Noll, S., Pierini, D., Pannella, M., & Savaglio, S. 2007, A&A, 472, 455
Peacock, J. A., et al. 2006, ESA-ESO Working Group on "Fundamental Cosmology," arXiv:astro-ph/0610906
Polletta, M., et al. 2007, ApJ, 663, 81
Prevot, M. L., Lequeux, J., Prevot, L., Maurice, E., & Rocca-Volmerange, B. 1984, A&A, 132, 389
Rowan-Robinson, M., et al. 2008, MNRAS, 386, 697
Salvato, M., et al. 2008, ApJ, 690, 1250
Sanders, D. B., et al. 2007, ApJS, 172, 86
Sawicki, M. J., Lin, H., & Yee, H. K. C. 1997, AJ, 113, 1
Schlegel, D. J., Finkbeiner, D. P., & Davis, M. 1998, ApJ, 500, 525
Scoville, N. Z., et al. 2007, ApJS, 172, 38
Silva, L., et al. 1998, ApJ, 509, 103
Steidel, C. C., et al. 2004, ApJ, 604, 534
Surace, J. A., Shupe, D. L., & Fang, F. 2004, VizieR Online Data Catalog, 2255, 0
Taniguchi, Y., et al. 2007, ApJS, 172, 9
Wang, L., & Steinhardt, P. J. 1998, ApJ, 508, 483
Wolf, C., et al. 2003, A&A, 401, 73
Wolf, C., et al. 2004, A&A, 421, 913
Zamojski, M. A., et al. 2007, ApJS, 172, 468